ADVANCED MATERIALS
www.advmat.de

Low Porosity Metallic Periodic Structures with Negative Poisson's Ratio

*Michael Taylor, Luca Francesconi, Miklós Gerendás, Ali Shanian, Carl Carson, and Katia Bertoldi**

The Poisson's ratio, ν, defines the ratio between the transverse and axial strain in a loaded material.[1] For isotropic, linear elastic materials, ν can neither be less than −1.0 nor greater than 0.5 due to empirical, work-energy, and stability considerations leading to the conditions that the shear modulus and bulk modulus have positive values.[2] Although materials with negative Poisson's ratio can exist in principle, most materials are characterized by $\nu > 0$ and contract in the directions orthogonal to the applied load when they are uniaxially stretched. The discovery of materials with negative Poisson's ratio (auxetic materials) that counterintuitively expand in the transverse directions under tensile axial load) is relatively recent.[3,4] Auxetic response has been demonstrated in a number of natural systems, including metals with a cubic lattice,[5] zeolites,[6] natural layered ceramics,[7] and ferroelectric polycrystalline ceramics.[8] Furthermore, following the pioneering work of Lakes,[9] several periodic 2D geometries and structural mechanisms to achieve a negative Poisson's ratio have been demonstrated. In all of these cases, careful design of the microstructure has led to effective Poisson's ratios $\bar{\nu} < 0$, despite the fact that the bulk materials are characterized by $\nu > 0$. In particular, it has been shown that auxetic behavior can be achieved in a variety of highly porous materials,[10] including foams with re-entrant[11–15] and chiral microstructure,[16,17] microporous polymeric materials,[18] networks of rigid units,[19] and skeletal structures.[20] Moreover, negative Poisson's ratio has also been shown in non-porous systems, such as laminates,[21,22] sheets assemblies of carbon nanotubes,[23] composites,[24] and polycrystalline thin films.[25]

An open area of research is within the important intermediate range between the extremes of non-porous and highly porous microstructures. Finding auxetic materials in this intermediate range greatly expands the number of structural applications, especially in those where specific porosities must be targeted. For example, in a gas turbine, there exist many perforated surfaces in the combustion chamber, the turbine section, the bypass duct, and the exhaust nozzle, which could all benefit from auxetic behavior. However, the target value for the through-thickness porosity is set by the required cooling performance or the acoustic damping function of the surface and typically ranges from 2% to 10%. The design of 2D systems capable of retaining a negative Poisson's ratio at such low values of porosity still remains a challenge.[26] Although it has been recently shown through an analytical/numerical study that diamond or star shaped perforations introduced in thin sheets can lead to auxetic behavior,[27] convincing experimental evidence of a low porosity auxetic material has not been reported. The goal of this work is to demonstrate one such low porosity structure in metal via numerical simulation and material testing.

Topology optimization is a mathematical approach that enables the best design of structures that meet desired requirements.[28] Using this technique, structures that exhibit negative Poisson's ratio have been designed,[29,30] and the results indicate that to achieve optimal auxetic response in low porosity structures, the microstructure must comprise an array of mutually orthogonal, very elongated holes.[31] Interestingly, auxetic response has also been observed in elastomeric porous structures where a pattern of mutually orthogonal ellipses is induced by buckling.[32]

Inspired by these observations, we focus on a very simple system – a square array of mutually orthogonal elliptical voids in a 2D metallic sheet characterized by low porosity. In particular, we investigate the effect of the hole aspect ratio on the macroscopic Poisson's ratio both through experiments and simulations. Our results demonstrate that, in this minimal system, the Poisson's ratio can be effectively controlled by changing the aspect ratio of the voids. For low aspect ratios, the structure is characterized by positive values of Poisson's ratio. However, as the aspect ratio increases, $\bar{\nu}$ is found to decrease monotonically eventually becoming negative. Remarkably, large negative values of $\bar{\nu}$ can be achieved through the adjustment of just one parameter, indicating an effective strategy for designing auxetic structures with desired porosity.

We start by exploring numerically through finite element simulations the effect of the pore aspect ratio on the

Dr. M. Taylor
School of Engineering and Applied Science
Harvard University
Cambridge, MA 02138, USA
Dr. L. Francesconi
Department of Material Science and Mechanical Engineering
Universitá degli Studi di Cagliari, Italy
Dr. M. Gerendás
Rolls-Royce Deutschland Ltd & Co KG, Dahlewitz, 15827, Blankenfelde-Mahlow, Germany
A. Shanian, C. Carson
Rolls-Royce Energy
9545 Cote de Liesse, Dorval, Québec, H9P 1A5, Canada
Prof. K. Bertoldi
School of Engineering and Applied Science
Harvard University
Cambridge, MA 02138, USA
E-mail: bertoldi@seas.harvard.edu
Prof. K. Bertoldi
Kavli Institute
Harvard University
Cambridge, MA 02138, USA

DOI: 10.1002/adma.201304464

macroscopic Poisson's ratio in a thin elastic plate characterized by a Young's modulus of 70 GPa and a Poisson's ratio of 0.35.[33] The commercial Finite Element package ABAQUS/Standard (Simulia, Providence, RI) is used for all the simulations. To reduce the computational cost and ensure the response is not affected by boundary effects, we consider two-dimensional, infinite periodic structures using representative volume elements (RVEs – see inset in **Figure 1**) and periodic boundary conditions. Each mesh is constructed using six-node, quadratic, plane stress elements (ABAQUS element type CPS6). In Figure 1a, we report the evolution of $\bar{\upsilon}$ as a function of the pore aspect ratio a/b for linear elastic sheets with porosity ψ = 2%, 3%, 4%, and 5%. The results clearly show the aspect ratio a/b of the holes strongly affects the lateral contraction/expansion of the structure. At aspect ratios near 1 (i.e., circular voids), the effective Poisson's ratio is nearly the same as the bulk material regardless of porosity. As the aspect ratio increases, $\bar{\upsilon}$ decreases and a transition from positive to negative values of $\bar{\upsilon}$ is observed. More precisely, for the case of structures with porosity ψ = 2%, 3%, 4%, and 5%, the transition from positive to negative values of $\bar{\upsilon}$ is observed at aspect ratios of approximately 29, 18, 14, and 11, respectively. Thus, it appears that significant auxetic behavior can be produced in metals at very low porosity, provided the void aspect ratio a/b is large enough.

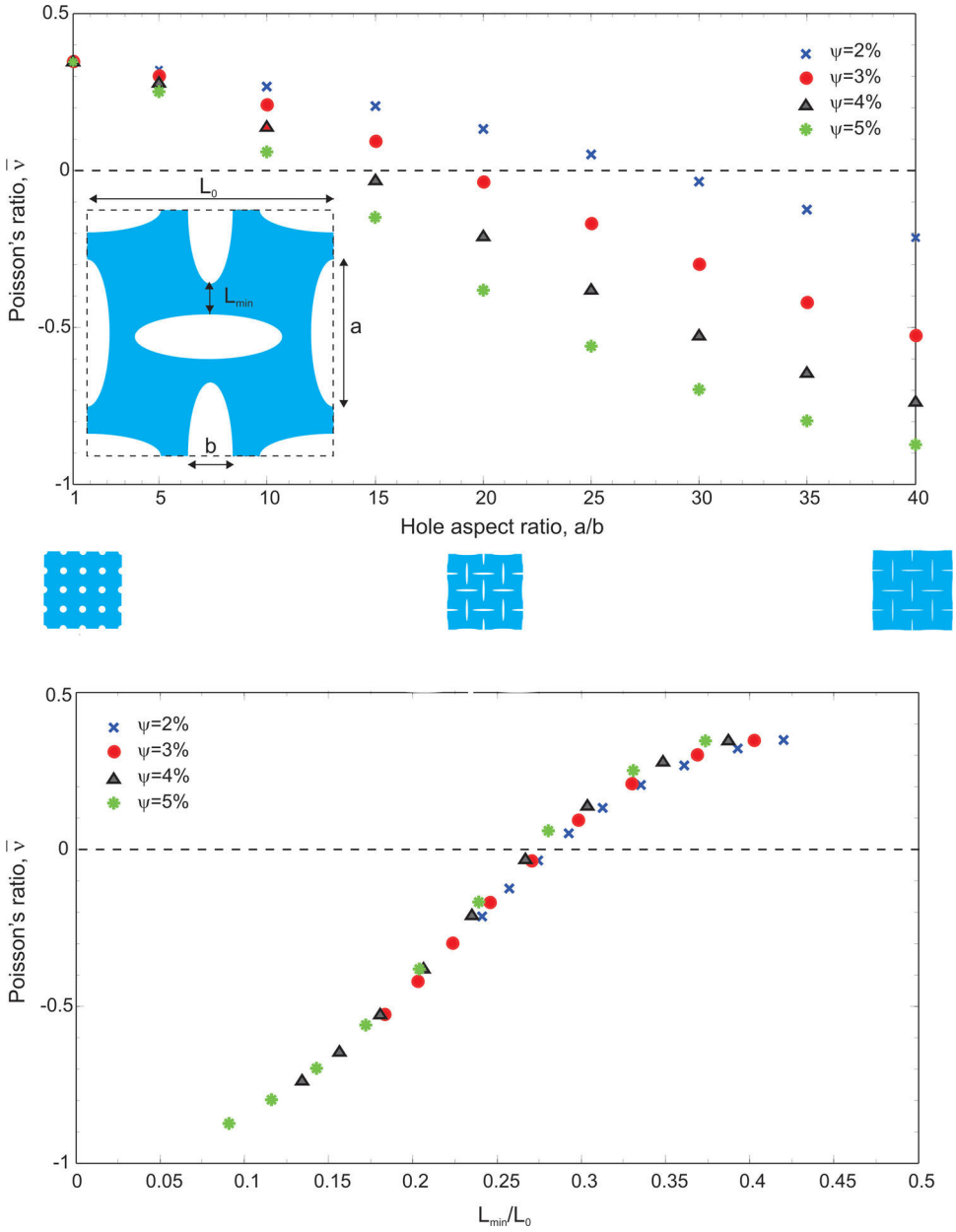

Figure 1. a) Results of the numerical investigation on the effect of the hole aspect ratio a/b for an infinite periodic square array in an elastic matrix. Four different values of porosity are considered. The RVE considered in the analysis is shown as an inset. b) All data collapse on a single curve when $\bar{\upsilon}$ is plotted as a function of L_{min}/L_0.

Adv. Mater. **2013**,
DOI: 10.1002/adma.201304464

Finally, it is worth noting the connection among the hole aspect ratio, sheet porosity, and the length L_{min} of the ligaments separating neighboring holes (see inset in Figure 1a)

$$L_{min} = \frac{L_o}{2}\left[1 - \left(1 + \frac{a}{b}\right)\sqrt{\frac{b}{a}\frac{\psi}{\pi}}\right] \quad (1)$$

where L_0 denotes the size of the RVE (see Figure 1a). In fact, when $\bar{v}$ is plotted as a function of $L_{\min} = L_0$ as shown in Figure 1b, all data remarkably collapse on a single curve, which can be used to effectively design structure with the desired values of Poisson's ratio and porosity. Thus, the ligament length appears to be the essential parameter controlling the auxetic response of these structures.

Next, we proceed by attempting to reproduce this auxetic behavior experimentally. In particular, we focus on two extreme cases and investigate the response of structures with porosity $\psi = 5\%$ and aspect ratios of $a/b = 1$ and $a/b = 30$. The experiments were performed on a 300 mm by 50 mm by 0.4046 mm aluminum (6061 alloy) cellular plates (see **Figure 2**), which were manufactured using the CNC milling process described in the Experimental Section. The gage section of the samples were patterned with circular holes with radius of $a = b = 3.154$ mm (see Figure 2, top) and elliptical holes with major and minor axis $a = 33.27$ mm and $b = 1.16$ mm (see Figure 2, bottom), respectively. Note that, due to the size of the end mill (with a diameter of 0.397 mm) required to manufacture the holes, the tips of exact ellipsoidal shapes were not produced, resulting in slightly lower aspect ratios, $a/b = 28.7$.

The samples are tested under uniaxial tension in an Instron biaxial testing machine equipped with a 10 kN load cell (pictures of the experimental set-up are shown in the Supporting Information). Similarly to previous studies where optical methods have been used to characterize the deformation in auxetic foams,[34–37] here the displacements within the samples are captured in detail using Digital Image Correlation (DIC). DIC is a technique by which displacements can be measured by correlating (via software) the pixels in several digital images taken at different applied loads.[38] In order for multiple frames to be correlated, every single part of the image must be uniquely detectable. This requires the surface of the samples to be covered in a non-repetitive, isotropic, and high-contrast pattern. In addition, the pattern must be fine enough to capture the desired displacement details consistent with the cameras and lenses used to capture the images. In our experiments, the surfaces of the samples are painted white with a fine distribution of black speckles using a Badger 150 airbrush and water-based paint leading to a density of approximately 3–6 pixels per speckle. The deformation of the sample is monitored using a high-resolution digital camera (1.3 MPixel Retiga 1300i with a Nikon optical lens system) and given our experimental setup the displacement accuracy is estimated to be approximately 500 to 700 nm.[38] The samples are loaded via displacement control at a rate 0.05 mm s^{-1} with the camera synchronized using the software Vic-Snap (Correlated Solutions) to capture images at a rate of 1 frame per second. Quantitative estimates of the deformation of the gage section of the sample are made using the image correlation software, Vic-2D (Correlated Solutions).

In addition to material testing, numerical investigations were performed on the experimental sample geometries using the nonlinear finite element code ABAQUS. Each mesh was constructed using ten-node, quadratic tetrahedral elements (ABAQUS element type C3D10) applied to the CAD model used to fabricate the samples. In order to accurately predict the material response near the voids, automatic adaptive mesh refinement is used, resulting in approximately 162,000 elements for

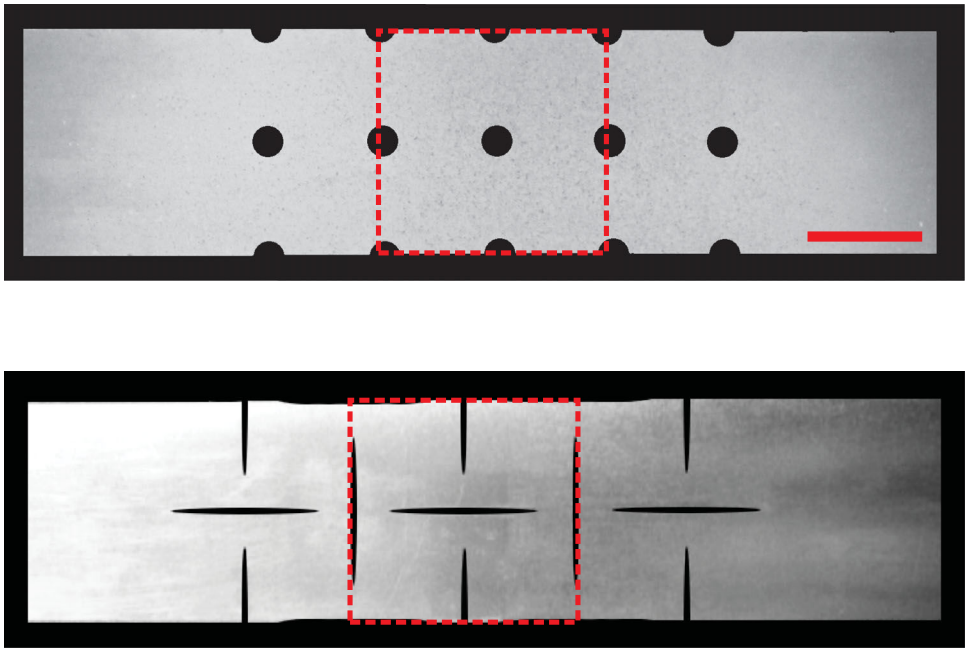

Figure 2. Samples comprising of a square array of (top) circular and (bottom) elliptical (with $\frac{a}{b} \cong 30$) holes in the undeformed configuration. The dashed rectangle represents region over which we perform the ensemble averaging. (Scale bar: 25 mm)

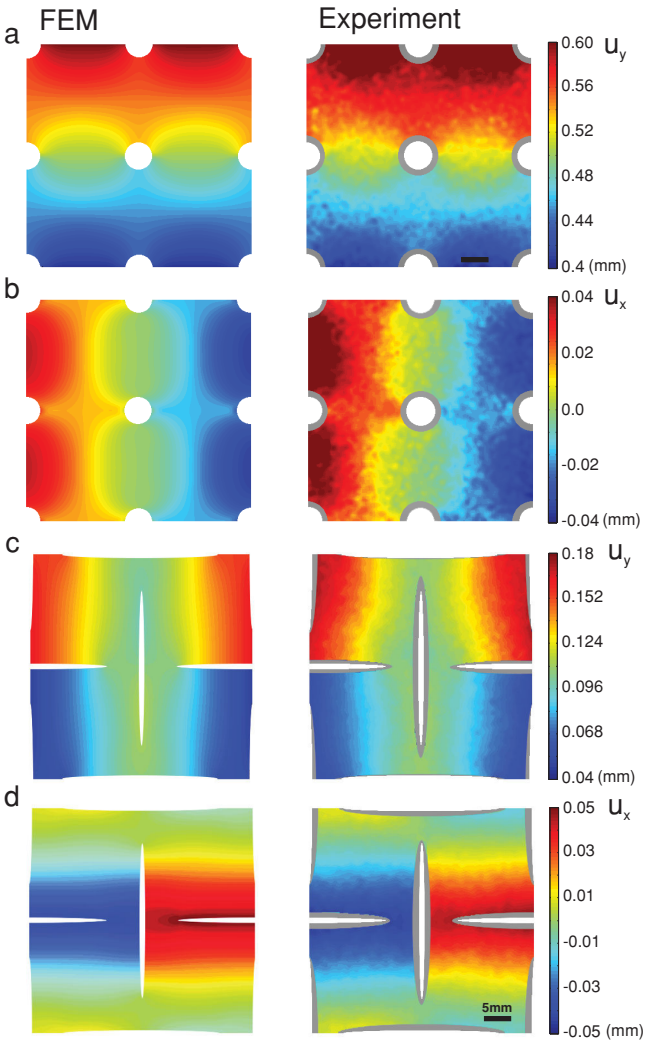

Figure 3. Contour maps for the horizontal (u_x) and vertical (u_y) component of the displacement field. Numerical (left) and experimental (right) results are quantitatively compared, showing excellent agreement. In (a) and (b), the applied strain is 0.34%, while in (c) and (d), the applied strain is 0.07%. Note that gray areas on experimental results show regions where DIC data could not be obtained.

the sample with circular voids and 119,000 elements for the sample with elliptical voids. The material is modeled as linearly elastic and perfectly plastic with a Young's modulus of 70 GPa and a Poisson's ratio of 0.35.[33] The yield stress is taken to be 275 MPa based on the experiments and is in agreement with available material data.[39] The applied experimental loading is approximated by fixing the translation at one edge and specifying a static displacement at the opposite edge. The remaining boundaries are traction free.

In **Figure 3**, we present both experimental (left) and numerical (right) results for the case of circular (top) and elliptical (bottom) pores. The specimen with circular pores is shown at an applied strain of 0.34%, while the specimen with elliptical holes is shown at an applied strain of 0.07%. Note that the applied strain is chosen to ensure the horizontal displacements are large enough to be accurately detected by DIC. As described later, the different deformation mechanisms taking place in the two structures considered in this study result in two different values of applied strain (additional results highlighting the effect of the applied strain on $\bar{\upsilon}$ are shown in the Supporting Information). To minimize the effect of boundaries, we focus on the central portion of the specimen (50 mm × 50 mm, see dashed red box in Figure 2) and report contour maps for the horizontal (u_x) and vertical (u_y) component of the displacement field. First, an excellent agreement is observed between simulation and experimental results. Moreover, the displacement maps reported in Figure 3 clearly show that the hole aspect ratio a/b strongly affect the mechanism by which the structure deforms. For the case of circular holes, the pores are found only to locally perturb the displacement field, so that the displacement field typical of the bulk material can be easily recognized (i.e. linear distribution of u_x and u_y in horizontal and vertical direction, respectively). In contrast, the array of elliptical holes is found to significantly affect the displacement field, completely distorting the linear distribution of u_x and u_y typical of the bulk material. Finally, it is worth noticing that the nature of the displacement contours is not affected by the level of applied strain, as shown in the Supporting Information.

Focusing on u_x, we can clearly see that the material is contracting laterally for the case of circular pores. In contrast, significant lateral expansion is observed for the samples with elliptical holes demonstrating auxetic behavior. To quantify the lateral deformation we compute the effective Poisson's ratio for these structures. In both the numerical and experimental results, we sample the displacement at 8 points along each of the four boundaries of the central regions shown as a dashed box in Figure 2. Each set of 8 points are averaged (arithmetic mean) to compute the average displacements at the boundaries: $\langle u_x \rangle^L$, $\langle u_x \rangle^R$, $\langle u_y \rangle^T$, $\langle u_y \rangle^B$, where superscript L, R, T, and B denote the left, right, top, and bottom boundaries, respectively. These average displacements are used to compute local strain averages

$$\langle \epsilon_{xx} \rangle = \frac{\langle u_x \rangle^R - \langle u_x \rangle^L}{L_o}, \quad \langle \epsilon_{yy} \rangle = \frac{\langle u_y \rangle^T - \langle u_y \rangle^B}{L_o} \tag{2}$$

L_0 = 50 mm denoting the distance between the top/bottom and left/right boundaries in the undeformed configuration. The local strain averages are then used to calculate an effective Poisson's ratio $\bar{\upsilon}$ as

$$\bar{\upsilon} = -\frac{\langle \epsilon_{xx} \rangle}{\langle \epsilon_{yy} \rangle} \tag{3}$$

For the deformations shown in Figure 3, the effective Poisson's ratios are reported in **Table 1**, where the values obtained from experiments and simulations are compared (additional numerical results for finite size samples characterized by

Table 1. Table summarizing the effective Poisson's ratio $\bar{\upsilon}$ of the two periodic structures measured from experiments and simulations.

	Experiments	FEM (finite size)	FEM (infinite size)
a/b = 1	0.33	0.34	0.34
a/b ≅ 30	–0.73	–0.76	–0.65

Adv. Mater. 2013,
DOI: 10.1002/adma.201304464

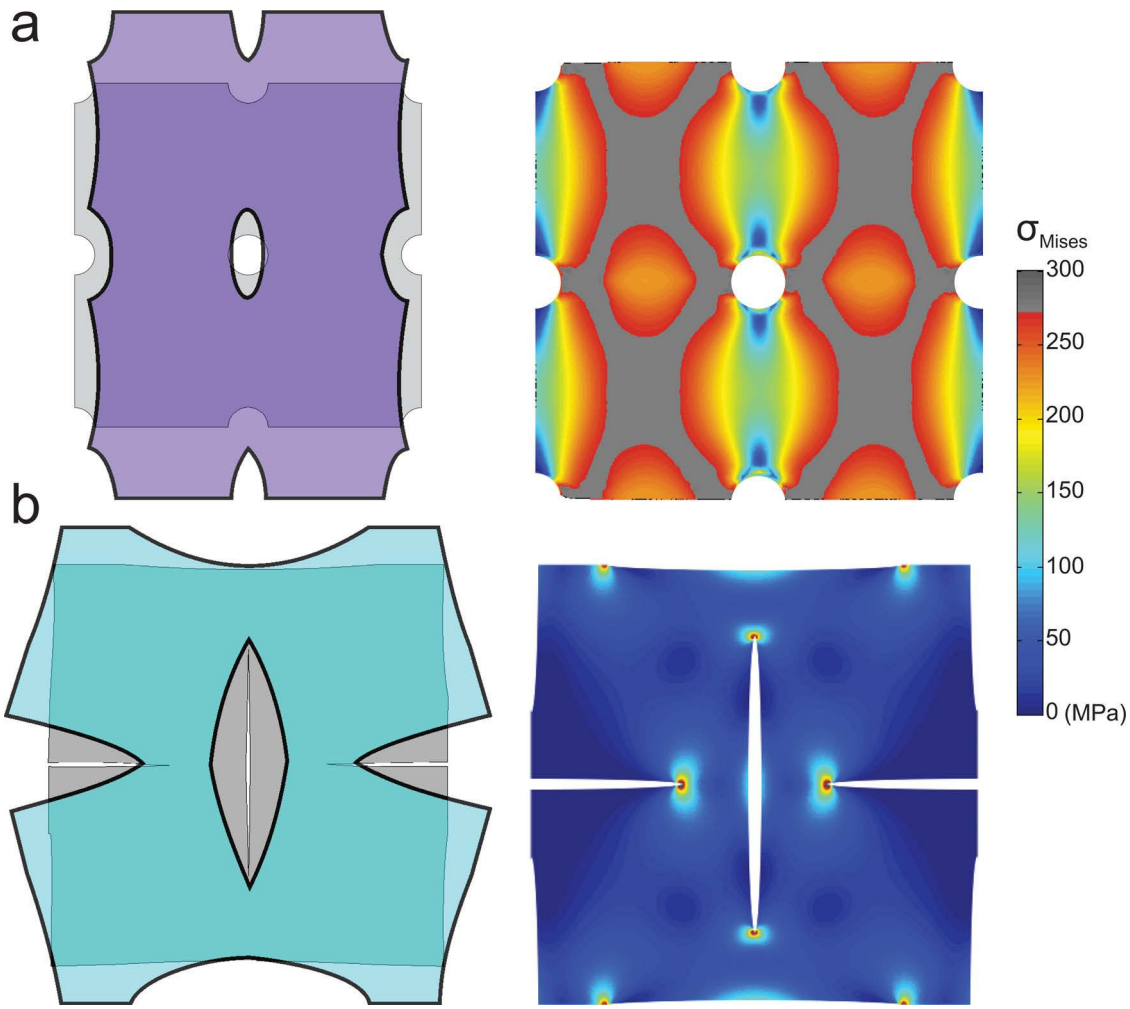

Figure 4. Effect of the pore aspect ratio *a/b* on the deformation of the structure. a) Deformed configuration superimposed over the unloaded configuration, with the displacement field in the deformed image scaled by a factor of 100. b) von Mises stress distribution with plastified areas colored gray. The applied strain is 0.34% and 0.07% for the structure with circular and elliptical holes, respectively.

different values of *a/b* are reported in the Supporting Information). For the numerical cases, results for infinite periodic domains (including the same elastic-plastic behavior used for the finite sample simulations) are also reported to ensure the response is not greatly affected by the boundary conditions. First, we note an excellent agreement between experiment and simulations. Second, the results very clearly indicate that high aspect ratio ellipses lead to a material characterized by a large negative value of $\bar{\upsilon}$. Interestingly, the numerical results for finite and infinite size domains are very close to each other, indicating that, although the size of the samples is quite small, the effect of the boundaries is not very pronounced. (Additional numerical results for samples of different size are shown in the Supporting Information.) Therefore, our results confirm that the hole aspect ratio can be effectively used to design structures with low porosity and large negative values of $\bar{\upsilon}$.

In **Figure 4**, we report numerical results to further highlight the effect of the pore aspect ratio *a/b* on the deformation of the material. In Figure 4a, we show the deformed configuration of central region of the samples superimposed over the unloaded configuration, with the displacement field in the deformed image scaled by a factor of 100. For the circular void sample, the deformation mechanism is stretching much the same as the mechanism in a similar void-less structure. By contrast, as previously shown in the analytical study by Grima and Gatt,[27] the deformation mechanism in the elliptical void sample is mostly due to rotation, leading to a negative Poisson's ratio. Finally, the completely different mechanism by which the two structures carry the load results in very different stress distributions within the material, as shown in Figure 4b, where we report the contour map for the von Mises stress. In the structures with circular pores, there are crosses that are highly stretched. These regions are yielded and deform plastically, as highlighted by the grey color in the contour map. In the case of elliptical holes, most of the structure experiences low values of stress and the deformation is found to induce rotation of the domain between holes. Stress is concentrated around the tips of the ellipses, but these can be easily reduced by carefully designing the tips to minimize the curvature.

In summary, our findings demonstrate a fundamentally new way of generating low porosity 2D materials with negative Poisson's ratio. We show that the effective Poisson's ratio can be effectively tuned by adjusting the aspect ratio of an alternating

pattern of elliptical voids. We have used numerical modeling to gain insight into the design of these structures as well as the underlying rotational mechanism causing the auxetic behavior at high void aspect ratios. These models have been verified using material testing with DIC, which has conclusively shown auxetic behavior in thin aluminum plates. We note that the structures investigated here exhibit two-dimensional cubic symmetry, meaning that the effective response is anisotropic. While further investigation of material symmetry is outside the scope of the current work, it is an important design issue. Thus, this work provides not only a guide for the simple design of auxetic materials but serves as a basis for future investigations into such areas as material symmetry and void shape optimization to minimize stress concentrations while maintaining a desired Poisson's ratio.

Experimental Section

Materials: Test samples were cut from 0.4046 mm thick 6061 Aluminum alloy plates. The bulk material has a Young's modulus of 70 GPa, Poisson's ratio of 0.35, and a yield stress of 275 MPa. In the numerical simulations, its behavior is modeled as linearly elastic and perfectly plastic.

Fabrication: Test samples were fabricated using a Haas OM2A CNC Machine together with a 2-flute ultra-duty coated (TiCn) carbide end mill (diameter = 0.39687 mm). Samples were fed into the mill at a speed of 2 inches per minute with a 0.003 inch depth of cut. Samples were designed in Solidworks CAD software (Dassault Systems) and imported to the CNC machine via SolidCAM.

Testing: Samples were tested at the MIT Impact and Crashworthiness Lab. Prior to testing, samples were coated in white water-based paint using a Badger150 airbrush. Contrast was added by spraying a fine pattern of black water-based paint to the recorded surface using the same airbrush. For the tests, samples were loaded into an Instron biaxial testing machine equipped with a 10 kN load cell using 5 cm wedge grips. The grips were secured using a steel block with aluminum spacers screwed together at a fixed torque resulting in constant contact pressure. Samples were illuminated uniformly in situ by means of tripod mounted diffused isotropic lighting. A Retiga 1300i camera (Nikon optical lens system) was mounted to a tripod and focused on a 80 mm by 60 mm rectangle in the central gage section of the samples providing digital imagery throughout the tests. The original image was then cropped to the 50 mm by 50 mm dimensions used in this study. The camera has a 1.3 MPixel resolution resulting in a pixel size of 6.7 µm by 6.7 µm. Samples were tested in tension at a rate of 0.05 mm s^{-1} with cameras triggered externally (via VicSnap) to capture 1 frame per second in synchronization with the applied Instron loading.

Supporting Information

Supporting Information is available from the Wiley Online Library or from the author.

Acknowledgements

This work has been funded by Rolls-Royce Energy. M.T., L.F. and K.B. thank Prof. Tomasz Wierzbicki and Stéphane Marcadet (MIT Impact and Crashworthiness Lab) for their support with the experiments.

Received: September 5, 2013
Revised: October 28, 2013
Published online:

[1] G. N. Greaves, A. Greer, R. Lakes, T. Rouxel, *Nat. Mater.* **2011**, *10*, 823.
[2] C. Truesdell, W. Noll, *The Non-Linear Field Theories of Mechanics*, 3rd Edition (ed: S. Antman), Springer-Verlag, Berlin **2003**.
[3] R. Lakes, *Adv. Mater.* **1993**, *5*, 293.
[4] K. E. Evans, A. Alderson, *Adv. Mater.* **2000**, *12*, 617.
[5] R. H. Baughman, J. M. Shacklette, A. A. Zakhidov, S. Stafström, *Nature* **1998**, *392*, 362.
[6] J. Grima, R. Jackson, A. Anderson, K. Evans, *Adv. Mater.* **2000**, *12*, 1912.
[7] F. Song, J. Zhou, X. Xu, Y. Xu, Y. Bai, *Phys. Rev. Lett.* **2008**, *100*, 245502.
[8] X. Tan, W. Jo, T. Granzow, J. Frederick, E. Aulbach, J. Rödel, *App. Phys. Lett.* **2009**, *94*, 042909.
[9] R. Lakes, *Science* **1987**, *235*, 1038.
[10] Y. Liu, H. Hu, *Sci. Res. Essays* **2010**, *5*, 1052.
[11] B. Xu, F. Arias, S. T. Brittain, X. M. Zhao, B. Grzybowski, S. Torquato, G. M. Whitesides, *Adv. Mater.* **1999**, *11*, 1186.
[12] C. Smith, J. Grima, K. Evans, *Acta Materialia* **2000**, *48*, 4349.
[13] U. Larsen, O. Sigmund, S. Bouwstra, *J. Microelec. Sys.* **1997**, *6*, 99.
[14] J. Schwerdtfeger, F. Schury, M. Stingl, F. Wein, R. F. Singer, C. Korner, *Phys. Stat. Sol. B* **2012**, *7*, 1347.
[15] F. Scarpa, P. Panayiotou, G. Tomlinson, *J. Strain Anal. Eng. Design* **2000**, *35*, 383.
[16] D. Prall, R. Lakes, *Inter. J. Mech. Sci.* **1996**, *39*, 305.
[17] A. Spadoni, M. Ruzzene, *J. Mech. Phys. Sol.* **2012**, *60*, 156.
[18] B. Caddock, K. Evans, *J. Phys. D: App. Phys.* **1989**, *22*, 1877.
[19] J. Grima, A. Alderson, K. Evans, *Phys. Stat. Sol. B* **2005**, *242*, 561.
[20] H. Mitschke, J. Schwerdtfeger, F. Schury, M. Stingl, C. Körner, R. F. Singer, V. Robins, K. Mecke, G. E. Schröder-Turk, *Adv. Mater.* **2011**, *23*, 2669.
[21] G. Milton, *J. Mech. Phys. of Sol.* **1992**, *40*, 1105.
[22] C. Herakovich, *J. Comp. Mat.* **1984**, *18*, 447.
[23] L. J. Hall, V. B. Coluci, D. S. Galvao, M. E. Kozlov, V. S. Zhang, O. Dantas, R. H. Baughman, *Science* **2008**, *320*, 504.
[24] D. Kochmann, G. Venturini, *Smart Mat. Struct.* **2013**, *22*, 084004.
[25] R. Mullen, R. Ballarini, Y. Yin, A. Heuer, *Acta Mater.* **1997**, *45*, 2247.
[26] Y. Prawoto, *Comp. Mat. Sci.* **2012**, *58*, 140.
[27] J. Grima, R. Gatt, *Adv. Eng. Mat.* **2010**, *12*, 460.
[28] M. Bendsoe, O. Sigmund, *Topology Optimization: Theory, Methods and Applications*, Springer-Verlag, Berlin **2003**.
[29] U. Larsen, O. Sigmund, S. Bouwstra, *J. Microelect. Sys.* **1997**, *6*, 99.
[30] J. Schwerdtfeger, F. Wein, G. Leugering, R. F. Singer, C. Korner, M. Stingl, F. Schury, *Adv. Mater.* **2011**, *23*, 2650.
[31] O. Sigmund, *Ph.D. Thesis*, Technical University of Denmark, **1994**.
[32] K. Bertoldi, P. M. Reis, S. Willshaw, T. Mullin, *Adv. Mater.* **2010**, *22*, 361.
[33] J. Tilley, *Understanding Solids: The Science of Materials*, Wiley, West Sussex, U.K. **2004**.
[34] C. Chen, R. Lakes, *J. Mat. Sci.* **1991**, *26*, 5397.
[35] S. McDonald, N. Ravirala, P. Withers, A. Alderson, *Scripta Mater.* **2009**, *60*, 232.
[36] F. Pierron, *J. Strain Anal. Eng. Des.* **2010**, *45*, 233.
[37] F. Pierron, S. A. McDonald, D. Hollis, J. Fu, P. J. Withers, A. Alderson, *Strain*. **2013**, *49*, 6, 467.
[38] M. A. Sutton, J. J. Orteu, H. Schreier, *Image Correlation for Shape, Motion and Deformation Measurements:Basic Concepts,Theory and Applications*, Springer, New York **2009**.
[39] M. F. Ashby, D. R. H. Jones, *Engineering Materials 1: An Introduction to their Properties and Applications*, 2nd Ed, ButterworthHeinemann, Oxford, U.K. **1996**.

ADVANCED MATERIALS

Supporting Information

for *Adv. Mater.*, DOI: 10.1002/adma. 201304464

Low Porosity Metallic Periodic Structures with Negative Poisson's Ratio

*Michael Taylor, Luca Francesconi, Miklós Gerendás, Ali Shanian, Carl Carson, and Katia Bertoldi**

Supplementary Material for
Low Porosity Metallic Periodic Structures with Negative Poisson's Ratio

Michael Taylor[a], Luca Francesconi[b], Mikós Gerendás[c], Ali Shanian[e], Carl Carson[e], Katia Bertoldi[a,d]

[a] *School of Engineering and Applied Science, Harvard University, Cambridge, MA 02138*
[b] *Department of Material Science and Mechanical Engineering, Universitá degli Studi di Cagliari, Italy*
[c] *Rolls-Royce Deutschland Ltd & Co KG, Dahlewitz, 15827 Blankenfelde-Mahlow, Germany*
[d] *Kavli Institute, Harvard University, Cambridge, MA 02138*
[e] *Rolls-Royce Energy, 9545 Côte de Liesse, Dorval, Québec, H9P 1A5*

S1. Full Samples

In this section, we show pictures of our experimental set-up as well as displacement contours of the full test specimens generated from finite element analysis

S1.1. Experiments

Pictures of our sample testing apparatus are shown in Figure S1. Samples were tested at the MIT Impact and Crashworthiness Lab headed by Professor Tomasz Wierzbicki. In the figure, both the samples with circular and elliptical holes are shown mounted in the Instron bi-axial testing machine.

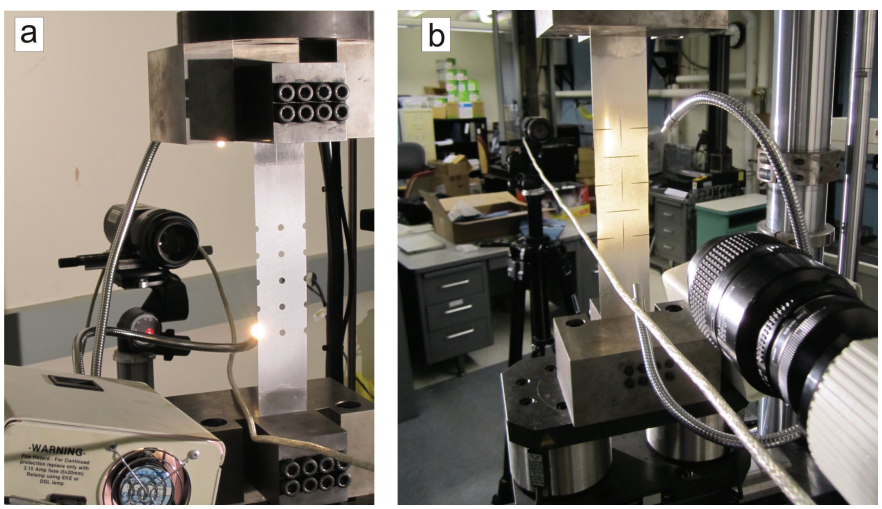

Figure S1: **Experimental system with test samples** *in situ*. The sample with circular holes is shown (a) in a view from the front. The camera and light are visible behind the sample. The sample with elliptical holes is shown (b) from the rear. The same camera and lighting are seen in the foreground.

S1.2. Full Simulation Contours

In the manuscript, displacement contour plots are shown for the central $50mm$ x $50mm$ region of both samples (see Fig. 3 in the manuscript). In Figures S2 and S3 of this document, we show the same displacement contour data generated from finite element simulations but within the context of the entire samples.

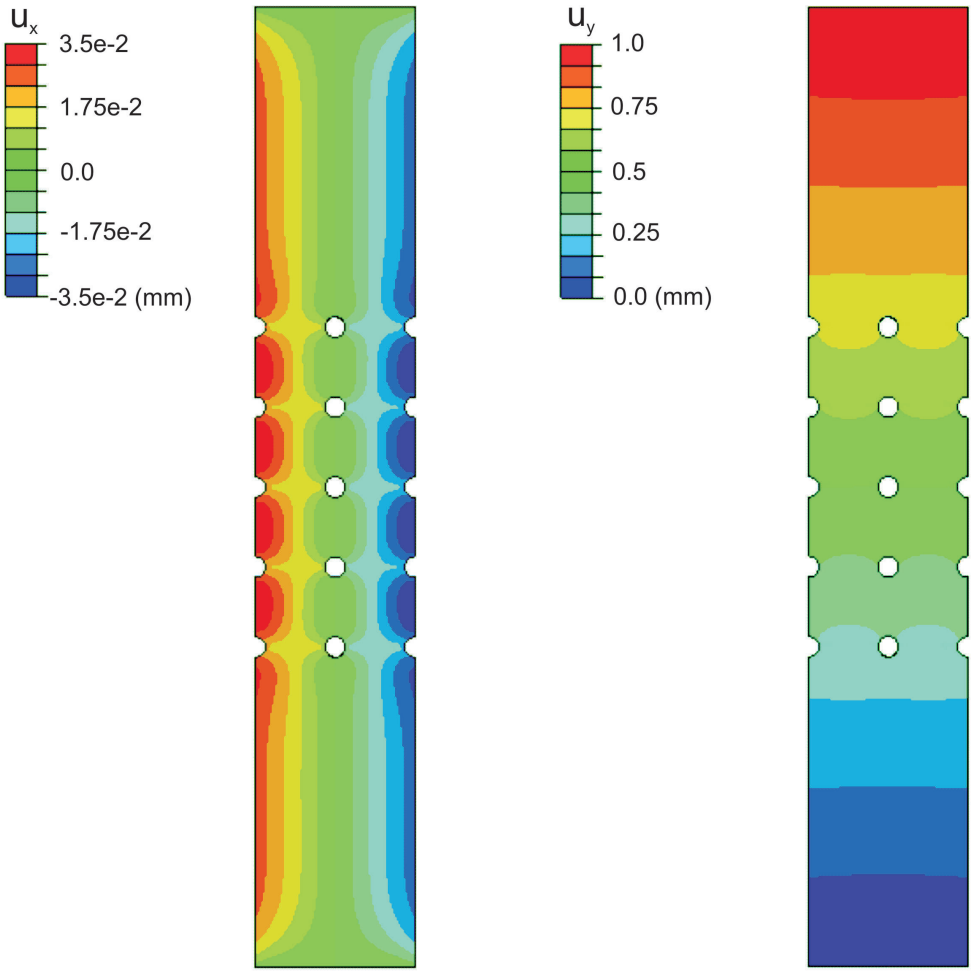

Figure S2: **Displacement contours for circular hole specimen.** Contour maps for the horizontal (u_x, left) and vertical (u_y, right) components of the displacement field are shown. Applied strain is 0.34% as in the manuscript. Scale bar corresponds to a length of $25mm$

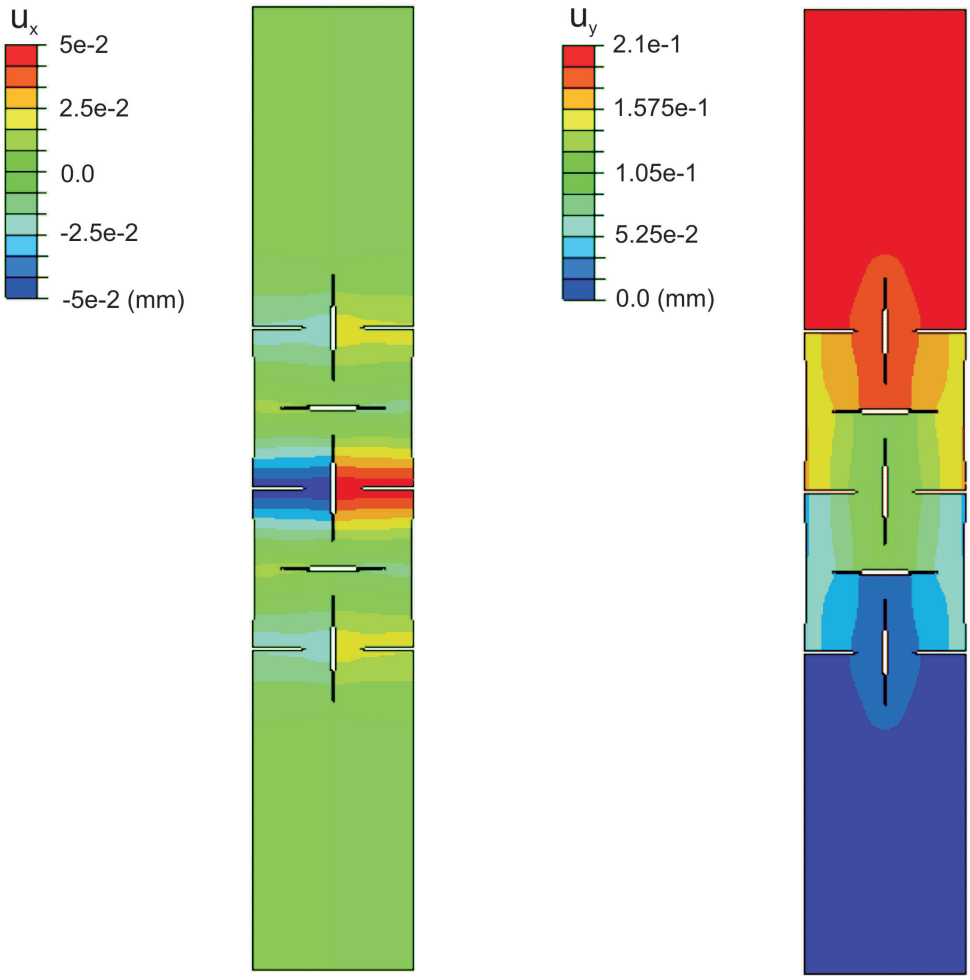

Figure S3: **Displacement contours for elliptical hole specimen with $a/b = 30$.** Contour maps for the horizontal (u_x, left) and vertical (u_y, right) components of the displacement field are shown. Applied strain is 0.07% as in the manuscript.

S2. Effect of Sample Size

In this section, we use finite elements to investigate the effect of using a larger sample on the calculation of effective Poisson's ratio. We take our original $300mm$ x $50mm$ sample (see Fig. 2 in the manuscript) and duplicate it twice in order to create a $300mm$ x $150mm$ body. We then repeat the same elastic-plastic analysis as we followed in the manuscript. Longitudinal strains of 0.34% and 0.07% are applied to the circular- and elliptical-holed samples, respectively. Full field displacement contours are shown Figures S4 and S6. To compute the Poisson's ratio, we again focus on a central $50mm$ x $50mm$ region (see dashed rectangular box in Figs. S4 and S6) and apply the method described in the manuscript. Close-up displacement contours of these regions are shown in Figures S5 and S7. The effective Poisson's ratio for the circular-hole and elliptical- hole (with $a/b = 30$)sample is computed to be 0.34 and -0.524, respectively, indicating that high aspect ratio ellipses lead to a material characterized by a large negative value of $\overline{\nu}$. Furthermore, it is important to note that these results are quite close to that reported in the manuscript for both the infinite periodic and finite size structures and confirm that, although the size of the samples is quite small, the effect of the boundaries is not dominating.

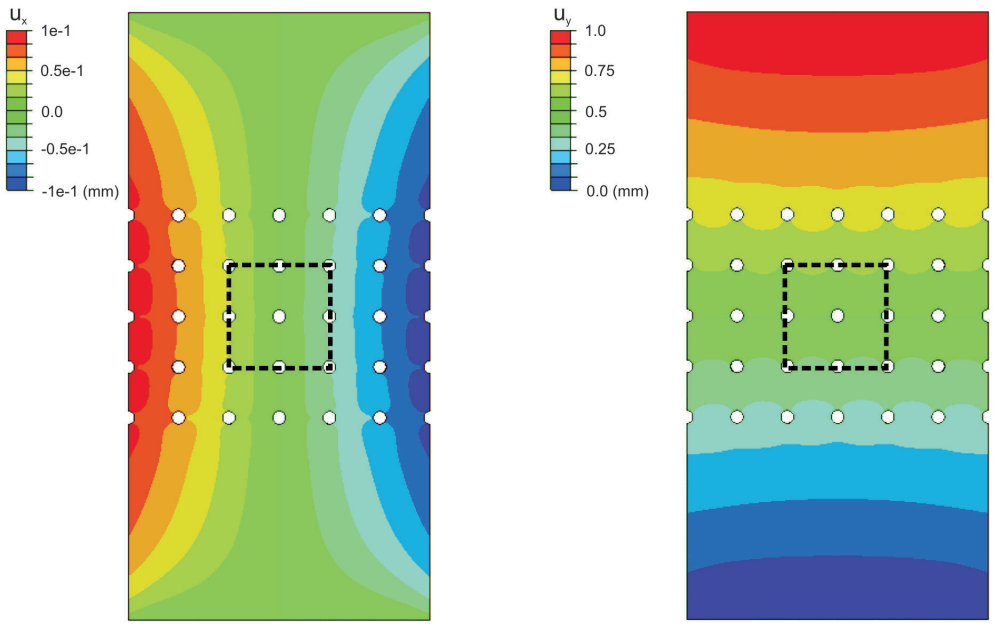

Figure S4: **Displacement contours for large circular hole specimen.** Contour maps for the horizontal (u_x, left) and vertical (u_y, right) components of the displacement field are shown. Applied strain is 0.34% as in the manuscript.

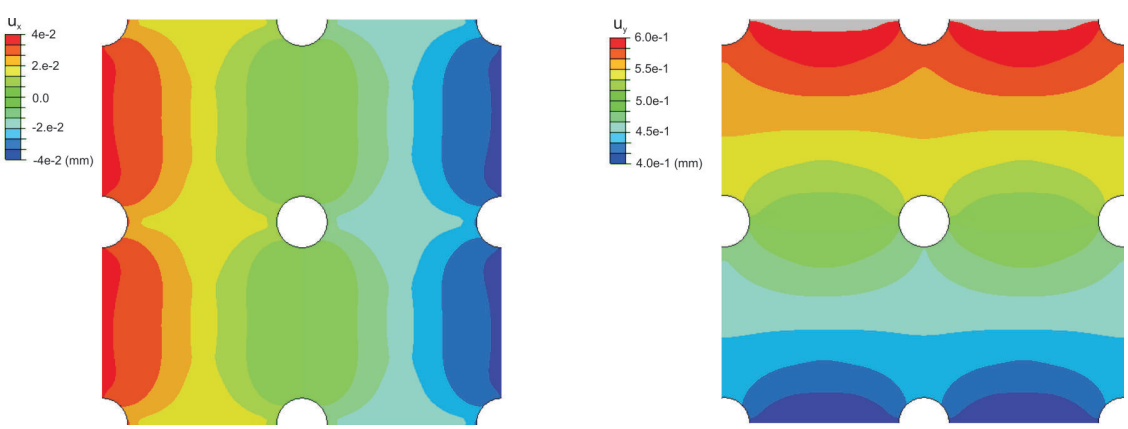

Figure S5: **Displacement contours for central region of large circular hole specimen.** Contour maps for the horizontal (u_x, left) and vertical (u_y, right) components of the displacement field are shown for the $50mm$ by $50mm$ central region highlighted in Figure 4. Range of contours set to match those of Fig. 3a and 3b of manuscript.

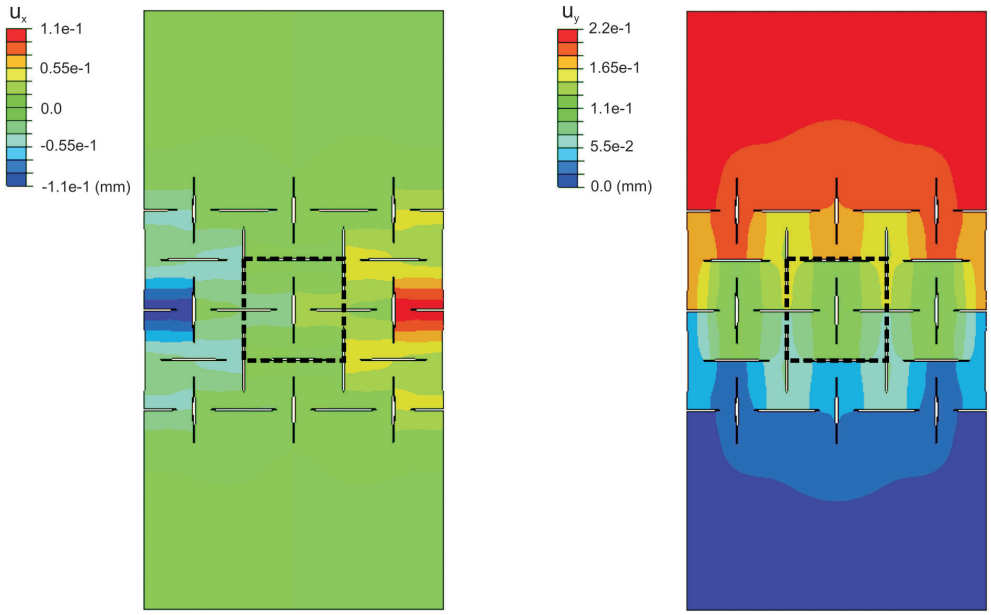

Figure S6: **Displacement contours for large elliptical hole with $a/b = 30$ specimen.** Contour maps for the horizontal (u_x, left) and vertical (u_y, right) components of the displacement field are shown. Applied strain is 0.07% as in the manuscript.

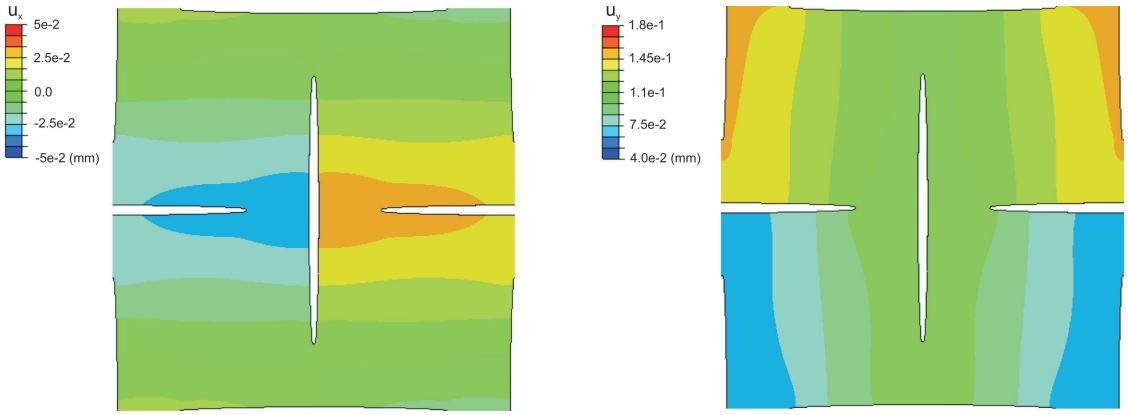

Figure S7: **Displacement contours for central region of large elliptical hole specimen.** Contour maps for the horizontal (u_x, left) and vertical (u_y, right) components of the displacement field are shown for the $50mm$ by $50mm$ central region highlighted in Figure 6. Range of contours set to match those of Fig. 3c and 3d of manuscript.

S3. Effect of Hole Aspect Ratio

In this section, we explore the effect of hole aspect ratio on the effective Poisson's ratio of the test sample geometry for a fixed porosity of 5%. We take our finite element models of the two test specimens (i.e., that with circular holes and that with elliptical holes) and subject them to a purely linearly elastic tensile deformation corresponding to an applied strain 0.1%. In addition, we create two new models having holes at the intermediate aspect ratio values of 10 and 20. These are subjected to the same deformation. For all four simulations, we compute the effective Poisson's ratio of the central $50mm$ x $50mm$ region using the same method detailed in the manuscript. These values are given in Table S1, showing good agreement with those of the corresponding infinite periodic structures reported in Fig. 1 in the manuscript. Displacement contours are shown in Figures S8 to S11.

	FEM (finite size)
a/b=1	0.35
a/b = 10	-0.1655
a/b = 20	-0.5504
a/b=30	-0.76

Table S1: Table summarizing the effective Poisson's ratio $\overline{\nu}$ of the four periodic structures measured from finite element simulations.

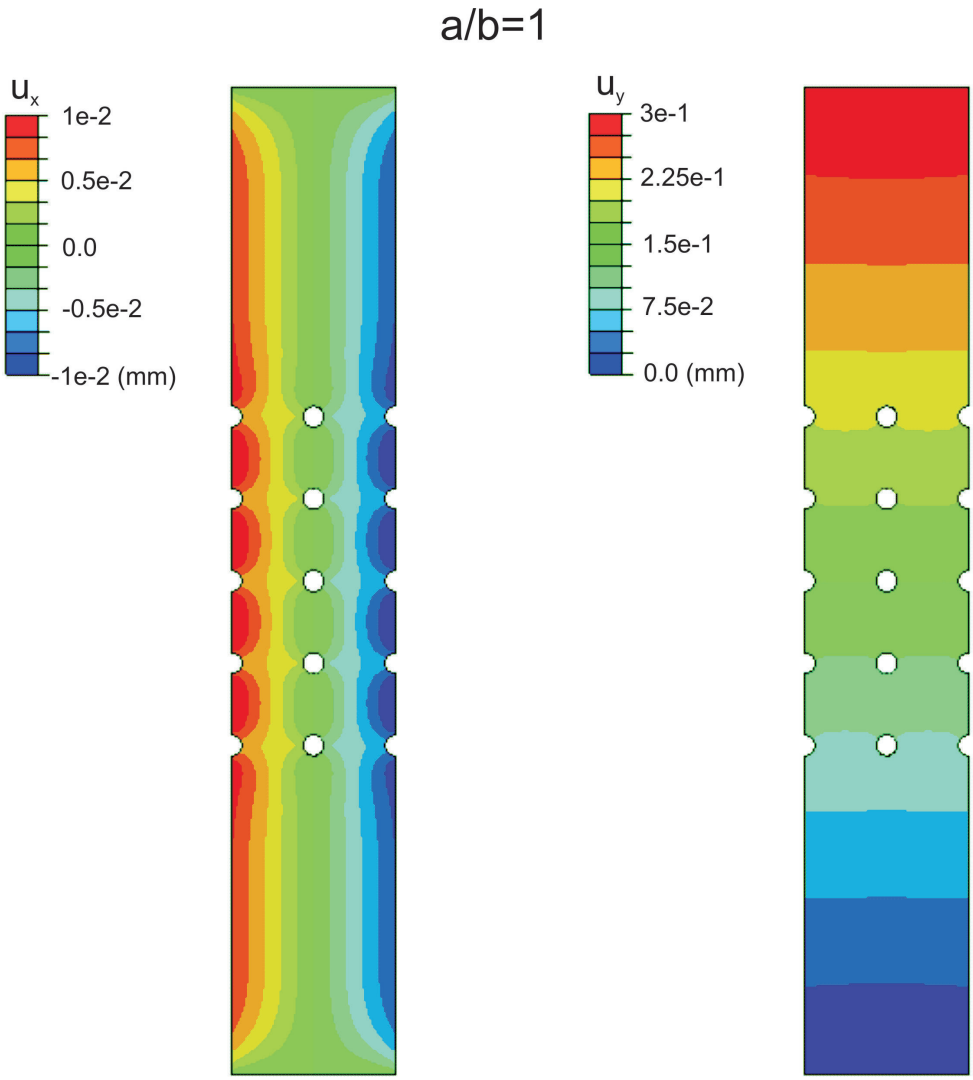

Figure S8: **Displacement contours for specimen with $a/b = 1$.** Contour maps for the horizontal (u_x, left) and vertical (u_y, right) components of the displacement field are shown. Applied strain is 0.1%.

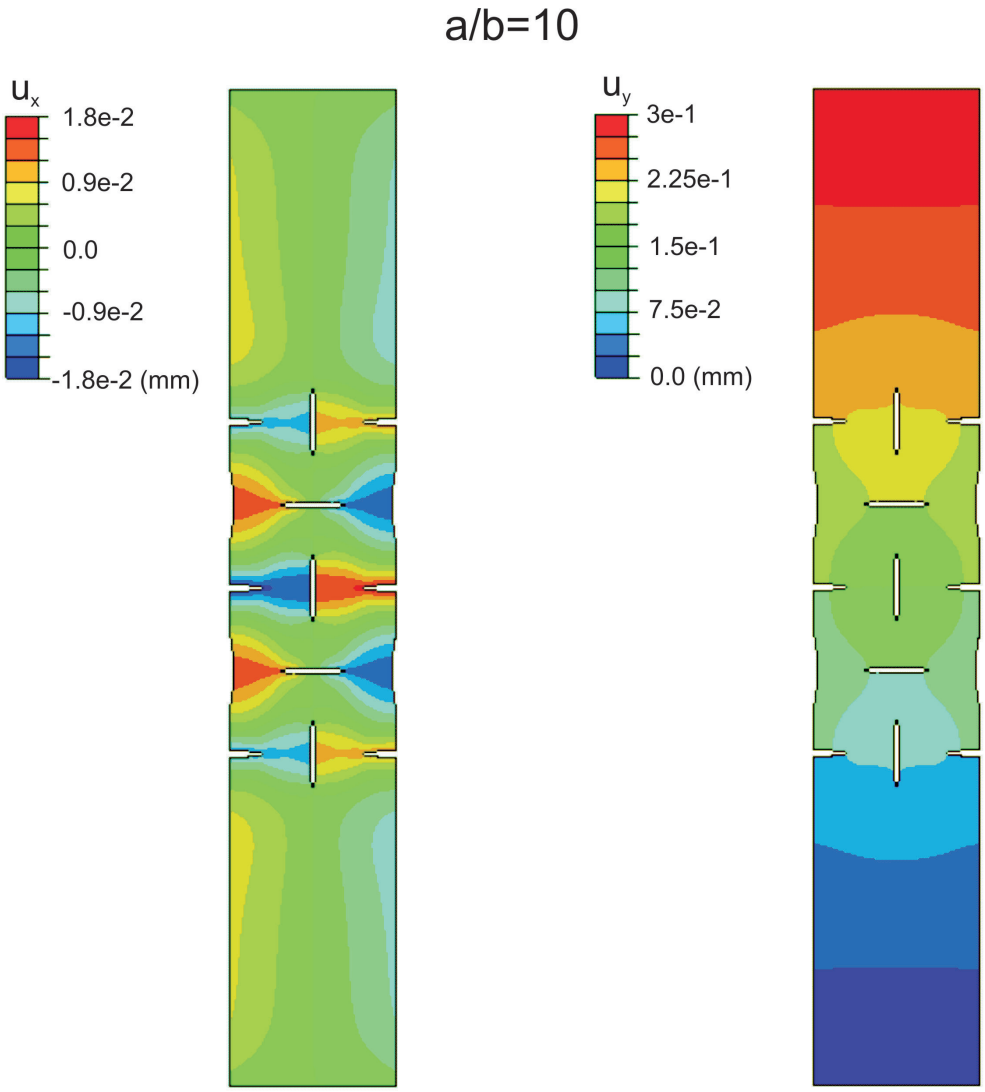

Figure S9: **Displacement contours for specimen with $a/b = 10$.** Contour maps for the horizontal (u_x, left) and vertical (u_y, right) components of the displacement field are shown. Applied strain is 0.1%.

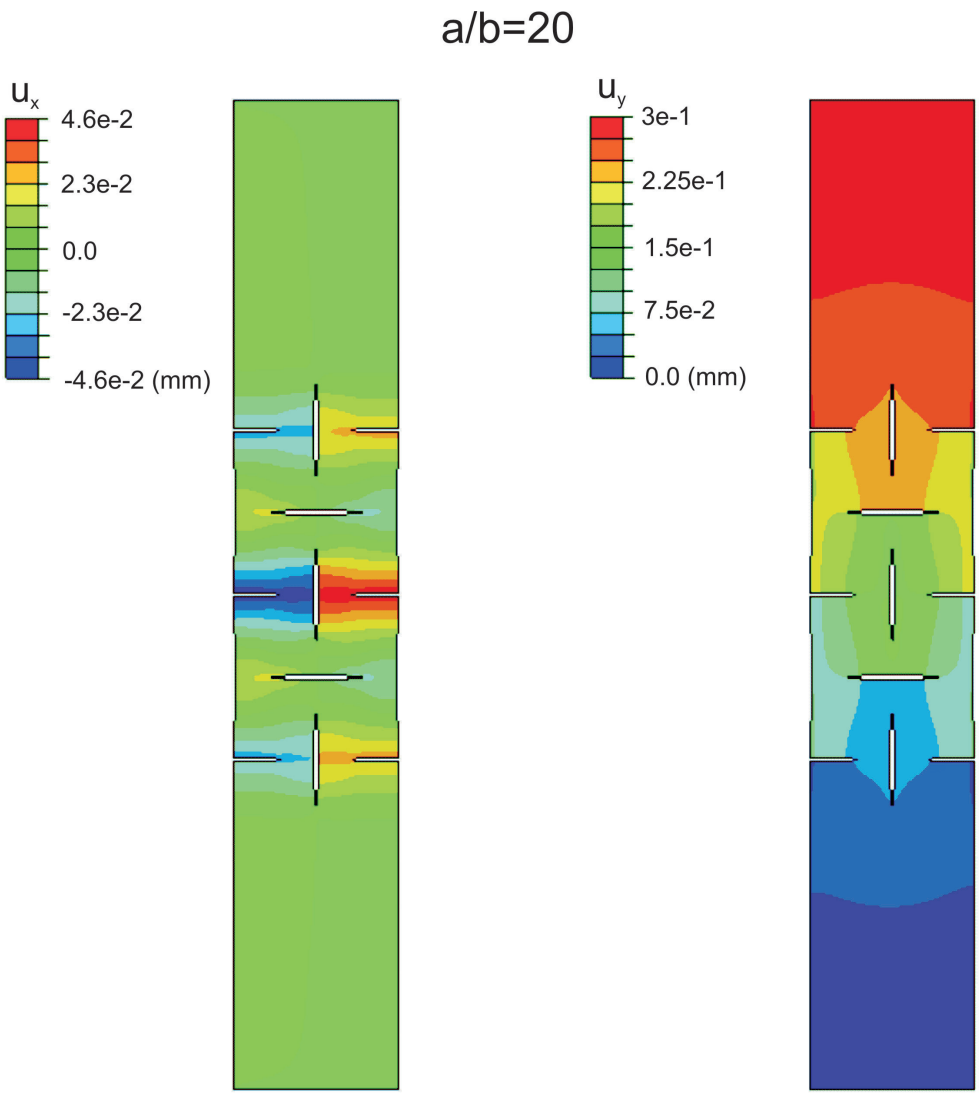

Figure S10: **Displacement contours for specimen with $a/b = 20$.** Contour maps for the horizontal (u_x, left) and vertical (u_y, right) components of the displacement field are shown. Applied strain is 0.1%.

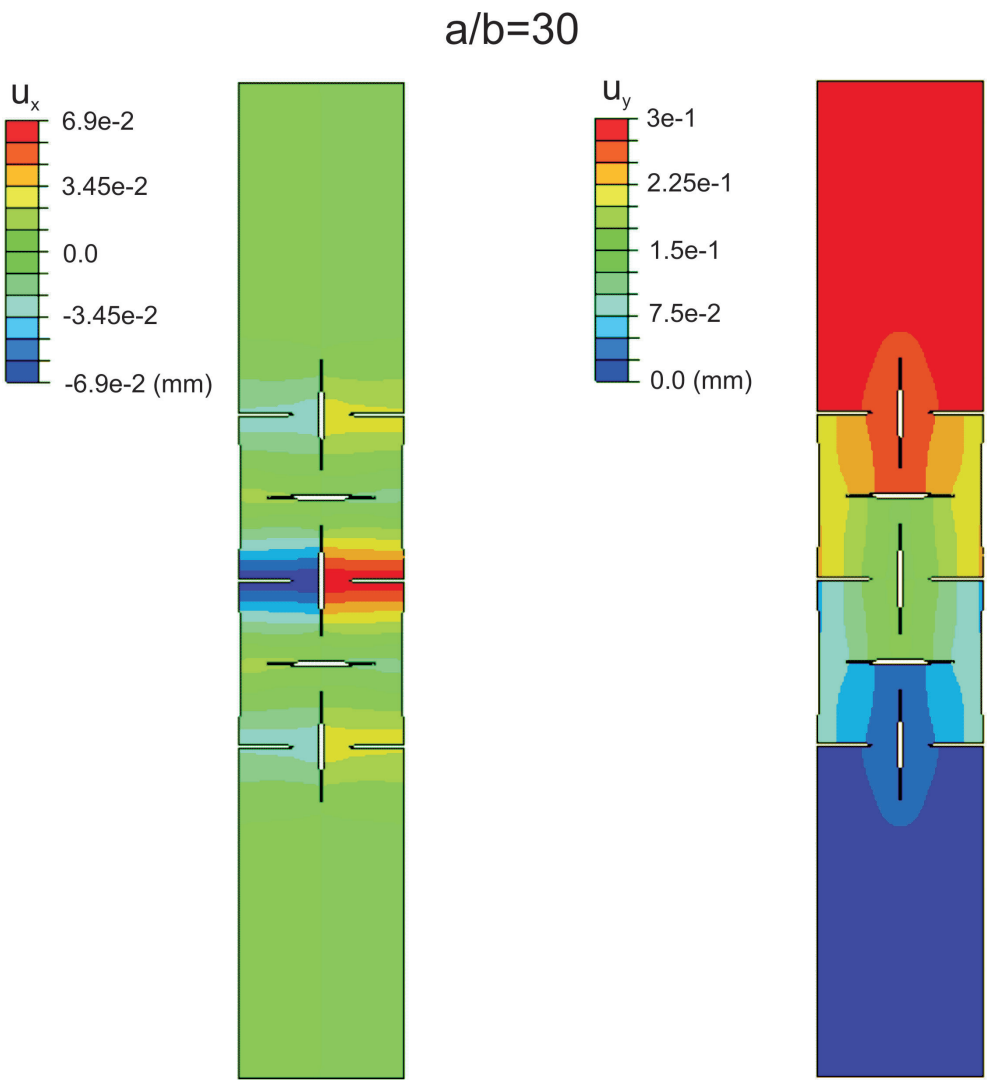

Figure S11: **Displacement contours for specimen with $a/b = 30$.** Contour maps for the horizontal (u_x, left) and vertical (u_y, right) components of the displacement field are shown. Applied strain is 0.1%.

S4. Effect of Strain

Here, we explore the effect of applied strain on the effective Poisson's ratio $\overline{\nu}$ and effective Young's modulus $\overline{E}$ for infinite periodic elastic-plastic structures performing the finite element analysis described in the manuscript. The results are plotted in Figure S12.

First, we note that under increasing strain the magnitudes of the effective Poisson's ratio for both structures moderately increases in absolute value. For the circular-hole structure, the Poisson's ratio become more positive approaching 0.5. For the elliptical-hole structure, the Poisson's ratio becomes more negative. Therefore, these results indicate that our auxetic structures are capable of retaining large negative values on Poisson's ratio also when increasing values of deformation are applied.

Focusing on the effective Young's modulus (Figure S12-b), we note that the elliptical-hole structure has an initial effective modulus ($400MPa$) roughly seven times less than the initial effective modulus of the circular-hole structure ($3040MPa$). For comparison, the bulk Young's modulus is $70GPa$. For both structures, the effective modulus decreases approximately by 80 % when a uniaxial strain of 0.02 is applied.

Finally, we show full field displacement contours for both the circular- and elliptical-holed specimen undergoing the same applied strain of .033% in Figures S13 and S14, respectively. Comparison with the plots included in the manuscript for two different values of strain clearly indicates that the nature of the displacement contours is not affected by the level of applied deformation.

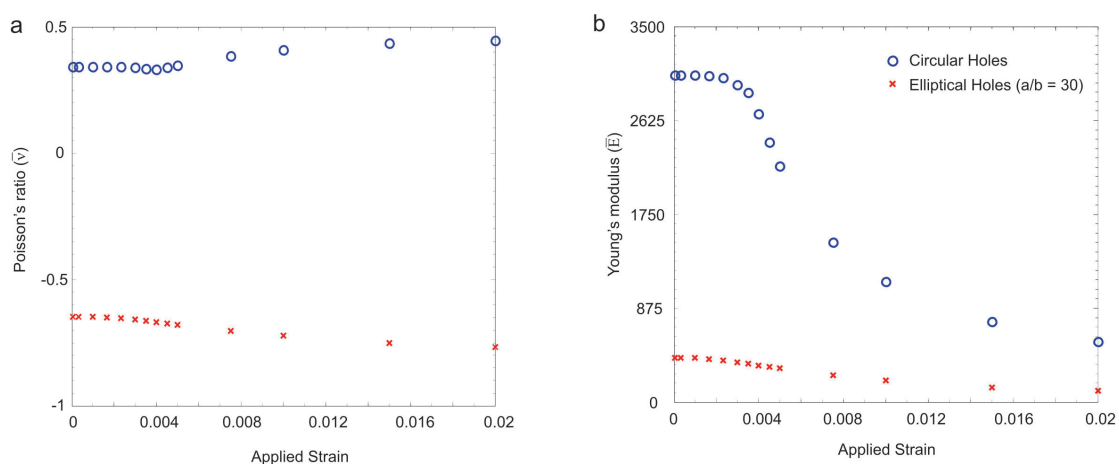

Figure S12: **Effect of strain on the effective properties.** (a) The effective Poisson's ratio $\overline{\nu}$ is shown as a function of applied strain for infinite periodic elastic-plastic circular and elliptical (with $a/b = 30$) microstructures. (b) The effective Young's $\overline{E}$ is shown as a function of applied strain for infinite periodic elastic-plastic circular and elliptical (with $a/b = 30$) microstructures.

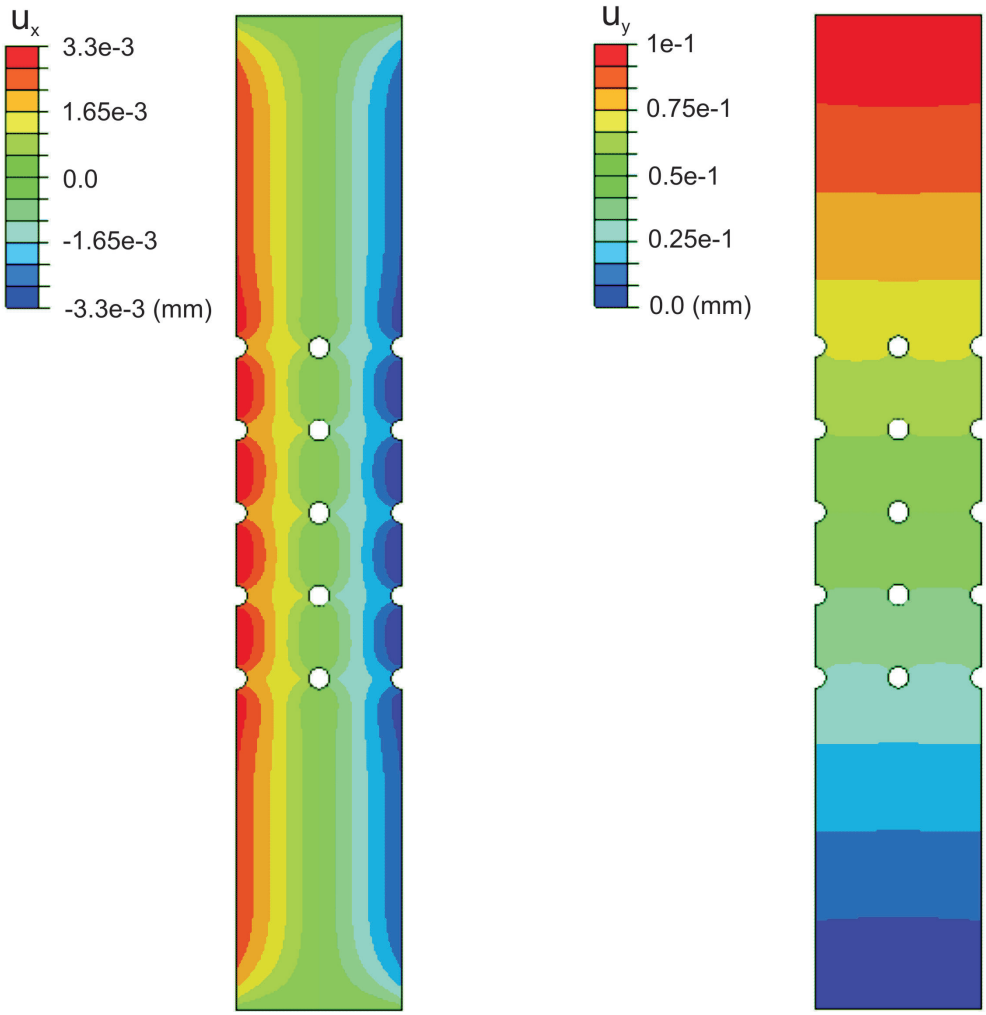

Figure S13: **Displacement contours for circular hole specimen.** Contour maps for the horizontal (u_x, left) and vertical (u_y, right) components of the displacement field are shown. Applied strain is 0.033% as in the manuscript.

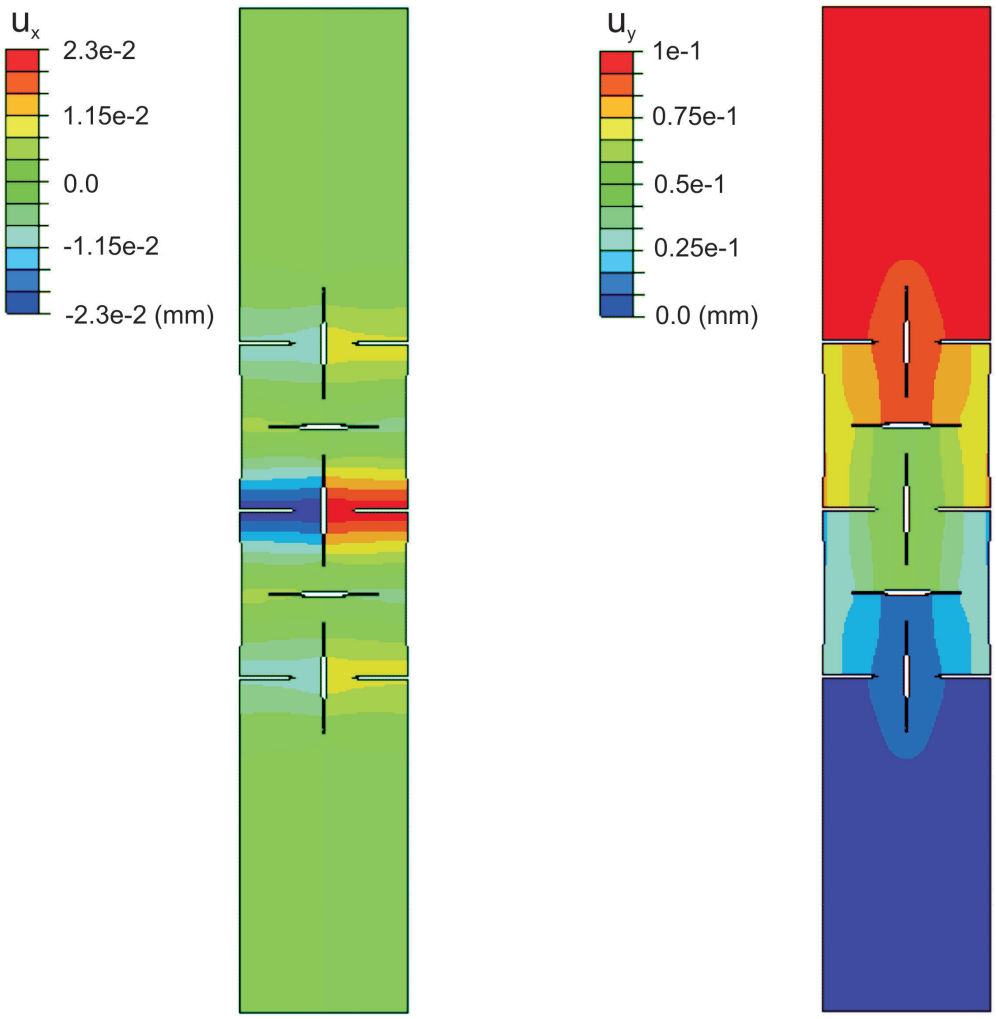

Figure S14: **Displacement contours for elliptical hole specimen with $a/b = 30$.** Contour maps for the horizontal (u_x, left) and vertical (u_y, right) components of the displacement field are shown. Applied strain is 0.033% as in the manuscript.